Bimetallic 3D Nanostar Dimers in Ring Cavities: Recyclable and Robust Surface-Enhanced Raman Scattering Substrates for Signal Detection from Few Molecules

Anisha Gopalakrishnan,[§] Manohar Chirumamilla,[§] Francesco De Angelis, Andrea Toma, Remo Proietti Zaccaria, and Roman Krahne*

Istituto Italiano di Tecnologia, Via Morego 30, 16163 Genova, Italy. [§]A. Gopalakrishnan and M. Chirumamilla contributed equally to the work.

ABSTRACT Top-down fabrication of electron-beam lithography (EBL)-defined metallic nanostructures is a successful route to obtain extremely high electromagnetic field enhancement *via* plasmonic effects in well-defined regions. To this aim, various geometries have been introduced such as disks, triangles, dimers, rings, self-similar lenses, and more. In particular, metallic dimers are highly efficient for surface-enhanced Raman spectroscopy (SERS), and their decoupling from the substrate in a three-dimensional design has proven to further improve their performance. However, the large fabrication time and cost has hindered EBL-defined structures from playing a role in practical applications. Here we present three-dimensional nanostar dimer devices that can be recycled *via* maskless metal etching and deposition processes, due to conservation of the nanostructure pattern in the 3D geometry of the underlying Si substrate. Furthermore, our 3D-nanostar-dimer-in-ring structures (3D-NSDiRs) incorporate several advantageous aspects for SERS by enhancing the performance of plasmonic dimers *via* an external ring cavity, by efficient decoupling from the substrate through an elevated 3D design, and by bimetallic AuAg layers that exploit the increased performance of Ag while maintaining the biocompatibility of Au. We demonstrate SERS detection on rhodamine and adenine at extremely low density up to the limit of few molecules and analyze the field enhancement of the 3D-NSDiRs with respect to the exciting wavelength and metal composition.

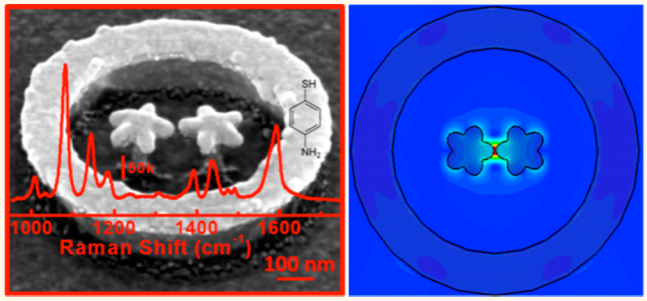

KEYWORDS: SERS · recycling · three-dimensional nanostructures · nanostar · dimer · ring cavity · bimetallic layer · sub-10 nm gap · single-molecule detection

Surface-enhanced Raman spectroscopy (SERS) is a versatile tool for the detection of biological or chemical analytes[1−4] that are deposited on metallic nanostructures at very low concentration, down to the limit of single/few-molecule detection (SMD).[5,6] In this context, the great advantage of SERS is its capability to provide molecular fingerprints of the analyte by label-free detection, *i.e.*, high specificity combined with high sensitivity. The high sensitivity results from the combination of chemical (CM) and electromagnetic (EM) enhancement. The former describes the charge transfer interaction from the electronic energy levels of the metal to the adsorbed molecules, therefore enhancing the Raman scattering crosssection of the molecule, leading to enhancement factors around 10−100.[7] On the other hand, the EM field enhancement crucially depends on the induced near-field intensity caused, for example, by localized surface plasmon resonances (LSPRs) in metallic nanostructures. Here, the dominating parameters are the shape and size of the nanostructures, interparticle distance, dielectric environment, and incident light polarization.[8] In this case the EM field can lead to enhancement factors up to the order of 10^6.[9] The extremely large SERS enhancement resulting from the combination of both CM and

* Address correspondence to roman.krahne@iit.it.

Received for review April 10, 2014 and accepted August 1, 2014.

Published online August 01, 2014
10.1021/nn5020038

EM enhancements counterbalances the low scattering cross-section of the Raman signal, enabling even single/few-molecule detection.[10] Despite some success of SMD with SERS, the fabrication of plasmonic nanostructures with extremely high EM enhancement is still a challenge, in particular with respect to wavelength tunability, homogeneity in field enhancement, and biocompatibility. Furthermore, the fabrication cost of SERS substrates and/or alternatively their recyclability for multiple uses are important issues. In fact, while bottom-up approaches can lead to low-cost SERS substrates with extremely high field enhancement, such as core–shell AgAu nanoparticles,[11] they do not provide good EM homogeneity. On the other hand, electron-beam lithography (EBL) combined with metal deposition and etching techniques allows for good control regarding the hot-spot design and extremely high EM enhancement. Among the best performing substrates are dimer structures, which lead to a highly localized EM enhancement in the nanosize gap.[12−14] Interestingly, the enhancement could be strongly increased by elevating the dimer structures from the substrate in a 3D geometry.[15] The disadvantage of this fabrication approach based on EBL is the high cost and the low throughput of the devices. In this paper we introduce elevated 3D nanostar dimers embedded in a ring structure, which integrate the advantages of extremely high EM enhancement at known location with excellent reproducibility, biocompatibility, tunable resonance wavelength, and facile recyclability that counterbalances the high fabrication cost inherent to EBL.

Ring-shaped nanostructures (circular reflectors) have been exploited during the past years for applications in a number of fields, such as electronics, optics, and magnetism.[16] The nanorings provide a uniform, enhanced electric field inside the cavity, similarly to a 3D nanoshell,[17] and have the advantage that the internal deposition of molecules is simpler than for nanoshells.[18−21] Circular reflectors that incorporate SERS nanostructures for increasing both the local electric field and the collection efficiency have been the subject of several reports.[16,22,23] The circular reflector creates a diffractive coupling[24] that reflects the light back to the ring center where the nanostructures are placed, hence increasing the local EM fields at this position.

Noble metallic nanostructures formed with Ag/Au metal layers are extensively used in various fields such as photonics, electronics, and sensing.[25−30] Ag yields higher field enhancement than Au;[31,32] however due to the Ag oxidation, Au nanostructures are preferred in biosensing owing to their low cytotoxicity, long-term stability, and biocompatibility. In order to exploit the advantages of both materials, bimetallic nanoparticles have been synthesized,[33−35] and a variety of combinations of Ag and Au bimetallic nanoparticles were developed by colloidal techniques.[36−39] Bimetallic nanostructures demonstrated improved performance in terms of stability, physical and chemical properties, and tunability of their resonance wavelength,[40,41] and therefore were extensively studied in SERS for biosensing.[42,43]

Sample recycling crucially depends on the applicability of cleaning processes, and in the case of 2D structures, processes such as plasma cleaning, ultrasonic cleaning, UV illumination, wet-etching, and thermal treatment can be used.[44−48] However, the above processes do not always guarantee a complete removal of the organic substances and possibly lead to damage of the plasmonic structures. Therefore, a facile routine to completely remove all organic materials without deteriorating the plasmonic performance remains a challenge.

We recently introduced three-dimensional plasmonic nanostar dimers for few-molecule detection by SERS spectroscopy, and their field enhancement was studied with respect to interparticle spacing (IPS) and pillar height.[49] In this work we developed this concept further by introducing (i) a metallic AgAu bilayer, leading to a higher field enhancement while conserving the biocompatibility of Au; (ii) larger interstructure spacing, which is possible due to the increased robustness of the nanostar dimer in the ring structure, which allows for single dimers in the detection spot; (iii) an additional EM field enhancement caused by the ring cavity; and finally (iv) a facile approach for recycling 3D structures *via* maskless etching and remetalization that guarantees complete removal of the analytes.

The bimetallic AgAu 3D nanostar dimer in a ring (3D-NSDiR) structure is shown in Figure 1. The 3D geometry was obtained by an isotropic reactive-ion etching (RIE) process masked by a specific Cr pattern that was previously defined by EBL. The hot spot in the dimer gap was decoupled from the Si substrate *via* silicon pillars that support the nanostars, and was placed in the center of a 3D ring cavity.

Numerical calculations were performed to optimize the structure geometry and to support the experimental data. The 3D-NSDiR structures were characterized with respect to the metal layer composition, star size, height, and incident light polarization. SERS performance and sensitivity were evaluated by using the nonfluorescent molecule *p*-aminothiophenol (pATP) as analyte, and more general versatility was demonstrated using also rhodamine (R6G) and adenine (DNA base) molecules at very low concentration. Finally, the recycling capability was quantified *via* repeated cycles of molecule chemisorption, SERS measurements, and cleaning *via* wet-chemical etching followed by metal evaporation, yielding a SERS enhancement factor of 10^7 (with respect to a planar Au film) in each cycle. Here the removal of the metal layer ensures complete removal of the analyte molecules, which even allows for reuse with different types of molecules. We emphasize

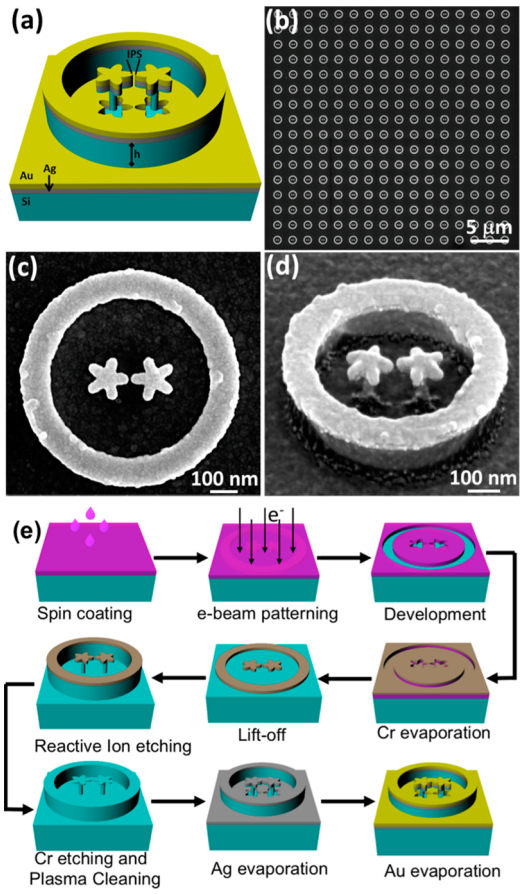

Figure 1. (a) Schematic representation of a AgAu 3D-NSDiR structure. (b) Normal-incidence SEM image of AgAu 3D-NSDiR structures. (c, d) Magnified image of a AgAu 3D-NSDiR structure with S5 size at normal incidence and at 52° tilted view, respectively. (e) Schemes illustrating the fabrication process.

that the maskless, large-area processing described here for regeneration of the SERS substrates is possible only for elevated 3D nanostructures.

RESULTS AND DISCUSSION

Plasmonic 3D-NSDiR structures with different star sizes (ranging from 100 to 240 nm for nanostar structures S1−S8, Table 1), with 5 nm dimer gap (IPS), and 150 nm height were fabricated by EBL and RIE processes, followed by 20 nm Ag and 20 nm Au metal deposition, as illustrated in Figure 1. The SEM images in Figure 1b−d demonstrate the overall fabrication quality in terms of reproducibility, homogeneity, and uniformity of the 3D-NSDiR structures. We chose a distance of 1 μm between neighboring 3D-NSDiR structures in order to ensure excitation of a single 3D-NSDiR in the detection area of the SERS measurements. The width of the ring was fixed at 130 nm, and the distance from the inner edge of the ring to the star edge was kept at 140 nm. The dimer gap was 5 nm, and its standard deviation (SD) measured from 20 nanostructures within the same substrate was 1 nm. Table 1 lists the geometrical parameters of the fabricated

TABLE 1. Geometrical Parameters of the Fabricated 3D-NSDiR Structures

3D-NSDiR notation	star size (L), nm	star branch length (B_L), nm	star branch width (B_w), nm	nanoring inner radius (R_1), nm
S1	100 ± 3	23 ± 2	38 ± 2	278 ± 3
S2	120 ± 2	27 ± 2	45 ± 2	295 ± 2
S3	140 ± 2	32 ± 3	48 ± 2	317 ± 2
S4	160 ± 2	43 ± 2	49 ± 2	335 ± 3
S5	175 ± 2	54 ± 2	50 ± 2	346 ± 2
S6	200 ± 2	63 ± 2	51 ± 2	372 ± 4
S7	220 ± 2	71 ± 2	52 ± 2	391 ± 2
S8	240 ± 2	76 ± 3	53 ± 2	407 ± 2

3D-NSDiR structures, where L, B_W, B_L, and R_I (see Figure 1) represent the star size, branch width, branch length, and inner radius of the nanoring, respectively. Figure SI1 in the Supporting Information (SI) shows SEM images of empty nanoring cavities.

The influence of both IPS and 3D elevation (*i.e.*, the pillar height) on the plasmonic field enhancement was discussed in ref 49. Briefly, the field enhancement increases with decreasing IPS, and increases with pillar height until it saturates at around 150 nm, indicating efficient decoupling of the hot spot from the substrate. Therefore, we chose here the smallest dimer gap size that could be reproducibly fabricated (IPS = 5 nm) and a pillar height of 150 nm.

Numerical Calculations. We have performed numerical calculations using CST-Microwave studio software for Au star dimers, AgAu star dimers, and AgAu star dimers in a ring (3D-NSDiR) with size parameters corresponding to the S5 configuration (see Table 1). The near-field distribution of the corresponding nanostructures in the $x-y$ plane (at the Si−metal layer interface) is shown in Figure 2, and plots in the $x-z$ plane are displayed in Figure SI2 of the SI. The field enhancement in the $x-y$ plane depends to a certain extent on its z position, in agreement with the literature.[50,51] The excitation wavelength was set to 830 nm with electric field polarization along the x-axis. The dielectric functions of the metal layers were taken from refs 52 and 53, and the dielectric constant of Si was set at $\varepsilon_{Si} = 15.21$. The outer edges of the nanostructures in the model were slightly rounded in order to match the fabricated structures, and convergence mesh analysis was applied to get stationary results. The field distribution on Au and AgAu 3D-nanostar dimers (NSDs) without a ring cavity is plotted in Figure 2a,b, evidencing that the maximum (localized at the center of the gap) is 4 times higher for the bimetallic configuration. This result can be understood by the relatively stronger plasmon resonance of Ag nanostructures with respect to Au.[31] The simulation of the 3D-NSDiR structure (Figure 2c,d) demonstrates the reflecting behavior of the ring cavity, leading to a very strong localization of the field enhancement in the dimer gap. In detail, we find an increase of the EM field

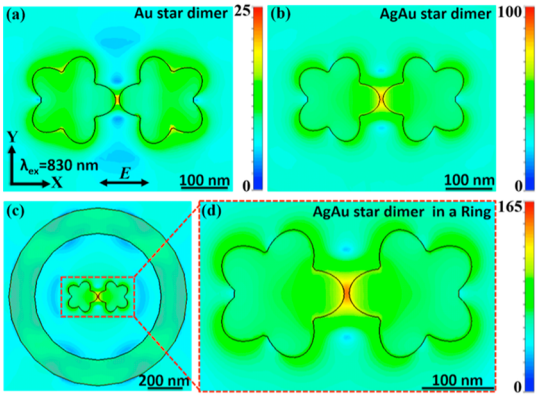

Figure 2. (a–c) Electric field distribution of a Au nanostar dimer, a AgAu nanostar dimer, and a AgAu nanostar dimer in a ring (3D-NSDiR), respectively, in the $x-y$ plane. (d) Magnified view of a 3D-NSDiR from (c). The scale bars represent the field enhancement, with the incoming field E_0 equal to 1.

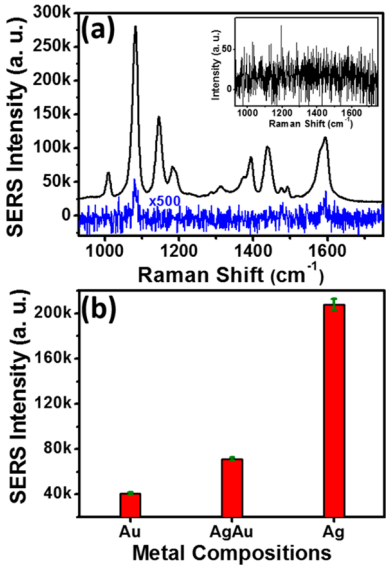

Figure 3. (a) Stokes SERS spectrum of pATP on AgAu 3D-NSDiR structures with S5 geometry. The blue trace shows the reference Raman spectrum of pATP on a planar AgAu film on the same substrate. The inset depicts the background Raman spectrum recorded from S5 AgAu 3D-NSDiR before chemisorption of pATP molecules. (b) SERS intensity of pATP as a function of metal layer composition. The green error bars show the standard deviation obtained from sets of ten measurements recorded from different structures within the same array. The excitation source, power, and accumulation time were 830 nm, 1.4 mW, and 30 s, respectively. The light was polarized along the interparticle axis.

by a factor of 1.65 with respect to the AgAu 3D-NSD configuration. We note that the simulation of an empty ring cavity (see Figure SI2c of the SI) results in a uniform electric field distribution inside the ring with an enhancement factor of 5, in agreement with the literature.[18] Overall, the EM enhancement of the 3D-NSDiR structure amounts to a factor of 165 in a highly localized hot spot. This value leads to a SERS enhancement,[54] expressed by the relation $(E_{loc}/E_0)^4$, on the order of 10^8. By considering also the chemical enhancement, a total SERS enhancement factor on the order of 10^{10} for AgAu 3D-NSDiR structures can be expected. We note that the hot-spot area in the center of the dimer gap (Figure 2d) will be used as active SERS area in the estimation of the experimental SERS enhancement factor.

SERS Measurements. We used pATP molecules chemisorbed from a 10 μM solution concentration in order to experimentally evaluate the SERS enhancement of the 3D-NSDiR structures. For all SERS measurements the polarization of the incident laser source was parallel to the IPS axis. Figure 3a shows a typical Stokes Raman spectrum recorded from a self-assembled monolayer of pATP molecules in the range 900–1750 cm^{-1} from a substrate with S5 AgAu 3D-NSDiR structures. All Raman bands of the spectrum match well with the characteristics of a pATP molecule.[55,56] Raman bands centered at 1077, 1180, and 1590 cm^{-1} correspond to a1 modes, whereas the peaks at 1140, 1390, and 1438 cm^{-1} correspond to b2 modes, and their assignment with respect to the molecular vibration modes is listed in Table SI1 of the SI. The blue trace in Figure 3a represents the reference Raman spectrum of a planar AgAu film that manifests only low-intensity bands at 1077 and 1590 cm^{-1}. The inset shows a featureless background Raman spectrum recorded from clean S5 AgAu 3D-NSDiR structures, *i.e.*, before chemisorption of pATP molecules, confirming the absence of surface contamination. The effect of nanostructure height on the SERS signal enhancement (see Figure SI3 of the SI) was demonstrated using 3D-NSDiR with a single Au metal layer and S8 geometry, on which pATP molecules were chemisorbed. As expected from our previous study, the signal intensity of the Raman band at 1077 cm^{-1} increases with increasing pillar height, until it saturates at around 150 nm.[49] SERS measurements from empty 3D ring structures are reported in Figure SI4 of the SI and show comparatively low enhancement with respect to the 3D-NSDiR, as expected from our simulations (Figure SI2c of the SI). Furthermore, the electric field, hence the SERS signal enhancement, depends significantly on the polarization of the incident light, resulting in a strong enhancement for light polarized parallel to the interparticle axis of the dimer (see Figure SI5 of the SI for the corresponding simulations and SERS spectra).

In order to elucidate the impact of the metal layer composition on the SERS signal enhancement, 3D-NSDiR structures with three different metal layers, Au, Ag, and AgAu, were fabricated with S5 geometry and a gap size of 20 nm. We chose deliberately a large gap size in order to minimize the impact of small gap size variations on the SERS intensity. Figure 3b shows the SERS intensity of the 1077 cm^{-1} band (with SD error bar, where the data were recorded from 10 different nanostructures on the same substrate) of pATP recorded from 3D-NSDiR structures that were coated with 20 nm of Au, 20 nm of Ag plus 20 nm of Au, and 20 nm of Ag, respectively. The corresponding SERS

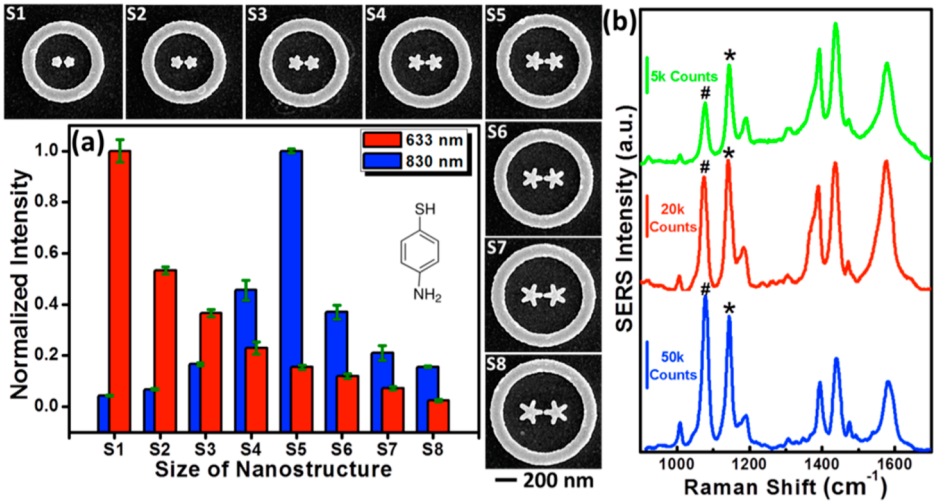

Figure 4. (a) SERS intensity from pATP molecules (chemisorbed from 10 μM solution) as a function of the 3D-NSDiR size, obtained from the 1077 cm^{-1} band for laser excitation at 633 and 830 nm. SEM images show 3D-NSDiR structures with sizes ranging from S1 to S8. The SERS intensity extracted from the other Raman bands with respect to star size is reported in Figure SI8 of the SI. The green error bars show the standard deviation obtained from sets of 10 measurements recorded from different structures within the same array. (b) SERS spectra of pATP (chemisorbed from a 10 μM concentration on S5 3D-NSDiR structures) recorded with laser excitation at 532 nm (green), 633 nm (red), and 830 nm (blue). The experimental parameters were 1.4, 0.25, and 4 mW for 830, 633, and 532 nm excitation wavelength, respectively, with an accumulation time of 30 s. Hash marks and asterisks indicate the a1 and b2 modes at 1077 and 1140 cm^{-1}, respectively.

spectra are reported in Figure SI6 of the SI. We found the strongest enhancement from the samples coated with a Ag layer, which can be rationalized by the plasmonic properties of Ag nanostructures.[32] On the other hand, the structures coated with a AgAu bilayer manifested lower enhancement; however they provide the considerable advantage of Au related to both biocompatibility and long-term stability. Furthermore, they show a factor 2 enhancement with respect to the 3D-NSDiR structures that were coated only by Au. For the AgAu 3D-NSDiR structures we obtained an average SERS enhancement factor of 4×10^7, by evaluating the peak at 1077 cm^{-1} recorded from pATP on nanostars with S5 geometry. This value corresponds to a reference Raman spectrum recorded from a planar AgAu film (the detailed calculation is reported in the SI). We note that planar AgAu films are already functioning as SERS substrates with an enhancement factor of at least 10^3;[49] therefore the absolute enhancement of the AgAu 3D-NSDiR structure can be estimated to be around 4×10^{10}.

The experimental SERS signal from a series of 3D-NSDiR with sizes ranging from S1 to S8 (see Table 1) was investigated with different laser excitation sources at 532, 633, and 830 nm wavelengths. Here, the IPS was 5 nm for all samples, and the structures were functionalized with pATP chemisorbed from a 10 μM solution concentration. Figure 4a shows the SERS intensity of pATP molecules on 3D-NSDiR structures as a function of the structure size for 633 (red bars) and 830 (blue bars) nm excitation wavelengths obtained from the 1077 cm^{-1} band. The SERS intensities were independently normalized with respect to the maxima recorded from S1 to S8 nanostructures. Typical SERS spectra from which the peak intensities were extracted are displayed in Figure 4b, and the 3D-NSDiR structures with different sizes (S1−S8) are shown by the SEM images. For 633 nm excitation wavelength we found the highest SERS signal for the smallest (S1) 3D-NSDiR structure and a continuous decrease in the SERS signal with increasing geometrical size. Therefore, the maximum of the plasmon resonance of the S1 structures can be expected around or below 630 nm. On the other hand, the SERS intensities recorded with 830 nm excitation wavelength show a maximum for the S5 NSDiR size, indicating good overlap of the plasmon resonance and the Raman band with the excitation laser wavelength.[57,58] This is confirmed by a simulation of the extinction spectrum of the S5 3D-NSDiR structures that manifests the maximum at around 820 nm (see Figure SI7 of the SI).

The characteristic peaks of pATP, the a1 and b2 modes[56,59,60] (indicated by hash and asterisk symbols), are evident in the spectra recorded at three different excitation wavelengths (532, 633, 830 nm) from S5 3D-NSDiRs. Interestingly, we observe a change in the relative intensities for the a1 and b2 modes with respect to the excitation wavelengths at 633 and 830 nm. This change can be explained by charge transfer from the metal to an affinity level of the adsorbed molecule, which is known to depend on the excitation wavelength.[61−63] We note that for the 532 nm excitation wavelength the relatively large imaginary part of the dielectric constant of Au leads to damping of plasmons in the 3D-NSDiR structure and therefore to lower signal intensity.[64,65]

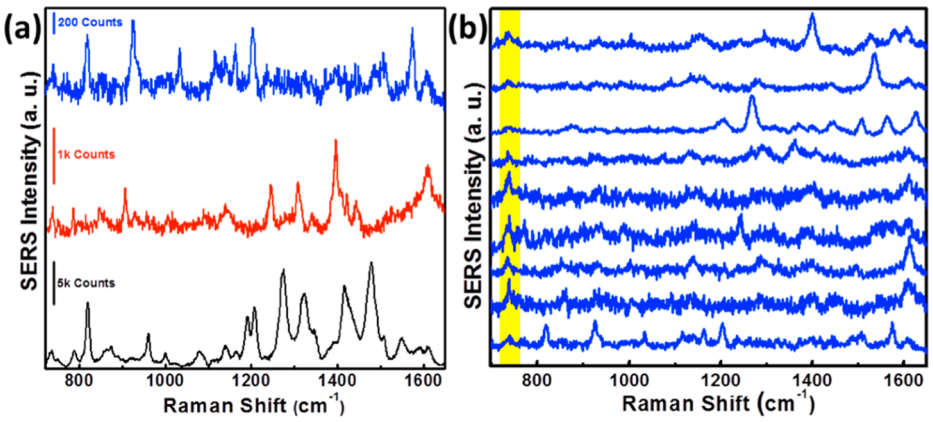

Figure 5. (a) SERS spectra recorded from adenine molecules chemisorbed on S5 3D-NSDiR structures from 1 μM, 1 nM, and 1 pM concentrations (shown as black, red, and blue traces, respectively). (b) SERS spectra of adenine (1 pM) recorded from nine different 3D-NSDiR structures of the same substrate. Laser excitation was at 830 nm (14 mW), and acquisition time was 3 s. The yellow bar in (b) highlights the characteristic 737 cm^{-1} Raman band of adenine.

3D-NSDiR Structures for High-Sensitivity Molecule Detection. We have explored the SERS detection sensitivity of 3D-NSDiR on two different nonresonant molecules (with respect to the laser source), adenine and R6G, that were chemisorbed from highly diluted solutions, namely, from 1 μM, 1 nM, and 1 pM concentration. Here, we used 3D-NSDiRs with S5 geometry coated with a AgAu bilayer, IPS of 5 nm, laser source at 830 nm, power 14 mW, and acquisition time 3 s. The experimental spectra obtained for adenine at different densities of molecular coverage are shown in Figure 5a. The chemisorption from 1 pM solution concentration led to only a few molecules per dimer, and the 50× objective with NA = 0.75 resulted in a spot size of ~1 μm, hence illuminating only a single 3D-NSDiR structure. The black trace in Figure 5a, recorded from molecules chemisorbed at 1 μM concentration, manifests the clearly distinguishable characteristic peaks of adenine, including the ring breathing mode at 737 cm^{-1}.[66−69] The full set of molecular vibration modes of adenine molecules is assigned in Table SI2 of the SI. Also for the substrates with lower molecular coverage (red and blue traces) the prominent adenine peaks can still be unambiguously recognized, even in the limit of a few molecules per hot spot obtained with pM concentration (blue trace). Figure 5b shows several spectra obtained from adenine molecules chemisorbed from 1 pM concentration recorded from nine different 3D-NSDiR structures on the same substrate. The characteristic vibrational band at 737 cm^{-1} (highlighted in yellow) is clearly evident in all spectra, showing some variation in peak intensity and position, which is characteristic for few-molecule detection.[69,70] We note that also the other peaks observed in Figure 5b can be assigned to adenine molecule vibrations.[66−69] The intensity and position of the peaks originating from the molecular vibrational modes are dominated by the orientation of the analytes adsorbed on the metal surface. From large molecule ensembles an average over all possible conformations is observed in the SERS spectra, while in a single-molecule experiment the differences in conformation (orientation of molecule with respect to the substrate and polarization of the laser beam) become evident. Therefore, the spectra presented in Figure 5b are an indirect proof of single/few-molecule detection capability of the 3D-NSDiR. Similar results obtained from a different molecule, R6G, are reported in Figure SI9 of the SI.

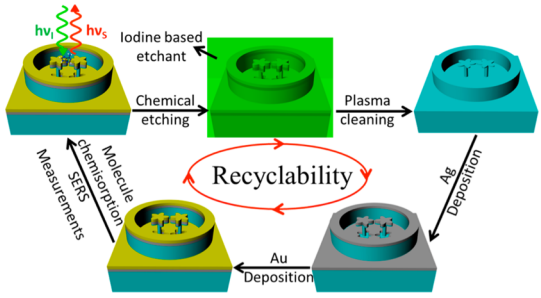

Figure 6. Illustration of the maskless recycling process that can be applied to 3D geometries such as the AgAu 3D-NSDiR nanostructures.

Recyclability of 3D-NSDiR Structures. 3D structures where the nanopattern is conserved in the geometry of the underlying substrate can be simply recycled by maskless processes such as metal etching, followed by metal redeposition, as illustrated in Figure 6. Importantly, the shape of the plasmonic structures is conserved if appropriate substrates and etchants are used. Concerning the 3D-NSDiR structures studied in this work, the bimetallic AuAg layers were removed by wet chemical etching with iodine, while the 3D Si structure maintained the nanostructure shape. We emphasize that the removal of the metal layer ensures also complete removal of all organic materials adsorbed on it (see Figure SI 10 in the SI for a comparison of plasma or piranha cleaning *versus* removal by wet etching plus metal redeposition). Then washing in DI water and 2-propanol and plasma-cleaning process were applied

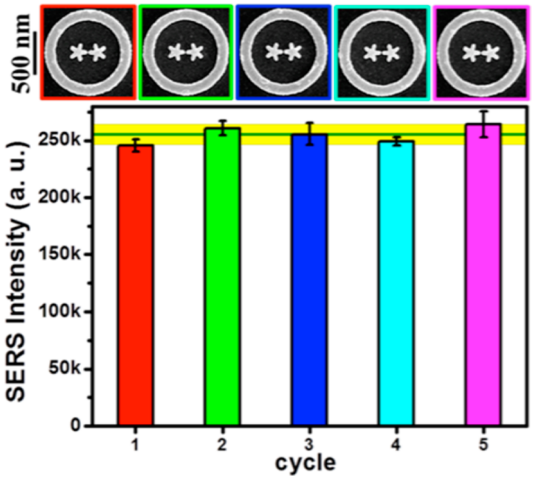

Figure 7. SERS intensity of the pATP band at 1077 cm^{-1} recorded after each recycling process from the same sample. The pATP molecules were chemisorbed from 10 μM solution concentration, and the experimental parameters were 830 nm excitation source at 1.4 mW power and 30 s acquisition time. The corresponding SEM images for each recycling step are shown in the top panel. The green error bars show the standard deviation obtained from sets of 10 measurements recorded from different structures within the same array.

to prepare the samples for the metal deposition. Finally, the bimetallic AuAg layer was redeposited by thermal evaporation of 20 nm of Ag, followed by 20 nm of Au.

We recycled the bimetallic 3D-NSDiR structures up to five times in order to evaluate the viability of this process. After each deposition of the metal layers, SEM images were taken to inspect the morphology of the 3D-NSDiR structures. The obtained SERS intensity (for the 1077 cm^{-1} band of pATP chemisorbed at 10 μM solution concentration) and SEM images to the nanostructures, and SEM images and SERS spectra for each recycling step are reported in Figure 7. We found good conservation of the nanostructure shape and high reproducibility in the SERS enhancement, corroborated by the small standard deviation of each series depicted by the black error bars in Figure 7. Within the different recycling steps the average SERS signal deviates no more than 10%, which is illustrated by the yellow horizontal region in Figure 7. For Raman spectra recorded at low concentration from recycled structures, see Figure SI 11 in the SI. This low-cost maskless recycling process is specific to the 3D geometry and cannot be applied to planar substrates.

CONCLUSIONS

We demonstrated that 3D-NSDiR structures discussed in this work have several unique advantageous properties for SERS, such as an extremely large enhancement factor of the order of 4×10^{10}, excellent control of hot-spot location and homogeneity, biocompatibility due to the exposed Au surface of the AgAu bilayer, and resonance wavelength tuning *via* nanostar size. In particular the elevated 3D geometry has multiple advantages over a 2D approach: (i) the plasmonic EM field enhancement is stronger due to efficient decoupling from the substrate; (ii) the minimum dimer gap size can be further reduced; and (iii) the substrates can be recycled *via* maskless and therefore cost-efficient processes. In particular the low-cost recycling possibility allows counterbalancing the high fabrication cost and time that are inherent to EBL-defined SERS nanostructures, and promises to make such elaborate substrates appealing candidates for commercial biosensing applications that require single/few-molecule detection sensitivity.

METHODS

Substrate Fabrication. 3D-NSDiR substrates were prepared by the combination of EBL (Raith 150-Two) and RIE (SENTECH). A cleaned p-type c-Si (100) wafer was spin-coated with a 300 nm thick layer of poly(methyl methacrylate) (PMMA, MicroChem Corp., 950 K) at 2000 rpm for 60 s. The substrate was transferred to a hot plate at 180 °C and baked for 8 min. The PMMA was patterned by EBL at a 30 kV accelerating voltage with 1 mC/cm^2 area dosage and 120 pA current. After exposure, the sample was developed in a solution of methyl isobutyl ketone and 2-propanol at a 1:3 ratio for 180 s at 4 °C. To create an etch mask for RIE, a 50 nm Cr layer was deposited by thermal evaporation (Kurt J Lesker system). Finally, ultrasonically assisted lift-off was performed to remove the excess resist and Cr metal. To obtain 3D nanostructures, RIE was used to etch silicon, using SF_6 (30 sccm) + C_4F_8 (32 sccm) as a gas mixture. The pressure, temperature, and power were 1 mTorr, 5 °C, and 18 W, respectively, leading to an etch rate of 100 nm/min. Finally, the Cr layer was removed by standard wet etching of Cr, and Ag/Au metal layers were deposited by thermal metal evaporation with a deposition rate of 0.3 Å/s. All SEM images were taken with FEI Helios Nano Lab 650.

Surface-Enhanced Raman Spectroscopy. SERS measurements were performed with a Renishaw inVia micro-Raman spectrometer using a 50× objective lens (NA = 0.75), resulting in a spot size with approximately 1 μm diameter. The individual 3D-NSDiR structures were identified *via* microscope optics, and the spot was centered on the structure under investigation. The Raman spectra were recorded with the excitation wavelengths at 830 nm (diode laser), 633 nm (HeNe gas laser), and 532 nm (Nd:YAG laser) with a spectral resolution of 1.5 cm^{-1} (in the near-infrared range) and 1.1 cm^{-1} (in the visible region). A thermoelectrically cooled charge-coupled device was used as detector. The system was calibrated with the first-order silicon LO phonon peak at 520 cm^{-1}, and spectra were recorded in back-scattering geometry. The laser spot was around 1 μm in diameter. All spectra were baseline corrected by a third-order polynomial using Wire software. The analyte molecules (pATP, R6G, and adenine) were purchased from Sigma- Aldrich.

Sample Preparation. The molecules were deposited on the SERS substrates by chemisorption from solutions with different concentrations, ranging from 10 μM to 1 pM. For pATP the solution was prepared by dissolving the molecule in ethanol, whereas R6G and adenine solutions were prepared using deionized water. Regarding chemisorption, the substrate was dipped in analyte solution for 20 min (for concentrations in the range of 1 nM to 10 μM), then rinsed in either ethanol (for pATP) or deionized water (for adenine and R6G), to remove the

unabsorbed molecules. Finally, the substrates were dried by nitrogen flow. In the case of 1 pM concentration the samples were left in solution for chemisorption up to 24 h, followed by rinsing and drying as previously described.

Numerical Calculations. CST Microwave Studio, which is based on the finite integration technique (FIT), has been used to calculate the electromagnetic field. This numerical approach is a powerful method for solving electromagnetic problems. It is especially capable of solving large and detailed structures. It is based on the solution of the Maxwell equations in their integral form. This approach allows the division of the overall simulation domain in smaller portions (units) with each of them being separately solved. Continuity relations among adjacent units provide the consistency of the general electromagnetic solution. We have adopted a tetrahedral mesh, which is especially suitable for curved surfaces. The FIT method allows the calculation in both near- and far-field; hence quantities such as electric-field distributions or extinction spectra can be efficiently determined by this numerical technique. Finally, in the present study, the convergence analysis approach has been especially stressed, due to the strongly irregular morphology of the structure. In this way, the error drops below 5% on the near-field calculations and less than 1% for the far-field results.

Conflict of Interest: The authors declare no competing financial interest.

Supporting Information Available: SEM images of empty ring cavities; calculated $x-z$ profiles of the field enhancement; SERS intensity *versus* pillar height; comparison of empty ring cavities with 3D-NSDiR structures; SERS spectra recorded from Au, Ag, and AgAu metal coatings; calculated extinction spectrum of 3D-NSDiRs; SERS enhancement factor calculation, SERS intensities as a function of 3D-NSDiR structure size, SERS spectra of R6G molecules at different concentration, tables specifying the assignment of Raman peaks from pATP, R6G, and adenine; SERS spectra recorded after oxygen plasma, piranha and recycle treatment. This material is available free of charge *via* the Internet at http://pubs.acs.org.

Note Added after ASAP Publication: This paper published ASAP on August 8, 2014. Author names were corrected in refs 41 and 65 and the revised version was resposted on August 13, 2014.

REFERENCES AND NOTES

1. Alvarez-Puebla, R. A.; Liz-Marzán, L. M. SERS-Based Diagnosis and Biodetection. *Small* **2010**, *6*, 604–610.
2. Lin, C.-C.; Yang, Y.-M.; Chen, Y.-F.; Yang, T.-S.; Chang, H.-C. A New Protein a Assay Based on Raman Reporter Labeled Immunogold Nanoparticles. *Biosens. Bioelectron.* **2008**, *24*, 178–183.
3. Lee, S.; Kim, S.; Choo, J.; Shin, S. Y.; Lee, Y. H.; Choi, H. Y.; Ha, S.; Kang, K.; Oh, C. H. Biological Imaging of Hek293 Cells Expressing Plcγ1 Using Surface-Enhanced Raman Microscopy. *Anal. Chem.* **2007**, *79*, 916–922.
4. Gopalakrishnan, A.; Malerba, M.; Tuccio, S.; Panaro, S.; Miele, E.; Chirumamilla, M.; Santoriello, S.; Dorigoni, C.; Giugni, A.; Proietti Zaccaria, R.; Liberale, C.; De Angelis, F.; Razzari, L.; Krahne, R.; Toma, A.; Das, G.; Di Fabrizio, E. Nanoplasmonic Structures for Biophotonic Applications: SERS Overview. *Ann. Phys.* **2012**, *524*, 620–636.
5. Nie, S.; Emory, S. R. Probing Single Molecules and Single Nanoparticles by Surface-Enhanced Raman Scattering. *Science* **1997**, *275*, 1102–1106.
6. Kneipp, K.; Wang, Y.; Kneipp, H.; Perelman, L. T.; Itzkan, I.; Dasari, R. R.; Feld, M. S. Single Molecule Detection Using Surface-Enhanced Raman Scattering (SERS). *Phys. Rev. Lett.* **1997**, *78*, 1667–1670.
7. Reilly, T. H.; Chang, S.-H.; Corbman, J. D.; Schatz, G. C.; Rowlen, K. L. Quantitative Evaluation of Plasmon Enhanced Raman Scattering from Nanoaperture Arrays. *J. Phys. Chem. C* **2006**, *111*, 1689–1694.
8. Kelly, K. L.; Coronado, E.; Zhao, L. L.; Schatz, G. C. The Optical Properties of Metal Nanoparticles: The Influence of Size, Shape, and Dielectric Environment. *J. Phys. Chem. B* **2002**, *107*, 668–677.
9. Otto, A. On the Significance of Shalaev's 'Hot Spots' in Ensemble and Single-Molecule Sers by Adsorbates on Metallic Films at the Percolation Threshold. *J. Raman Spectrosc.* **2006**, *37*, 937–947.
10. Etchegoin, P. G.; Le Ru, E. C. A Perspective on Single Molecule SERS: Current Status and Future Challenges. *Phys. Chem. Chem. Phys.* **2008**, *10*, 6079–6089.
11. Kumar, G. V. P.; Shruthi, S.; Vibha, B.; Reddy, B. A. A.; Kundu, T. K.; Narayana, C. Hot Spots in Ag Core–Au Shell Nanoparticles Potent for Surface-Enhanced Raman Scattering Studies of Biomolecules. *J. Phys. Chem. C* **2007**, *111*, 4388–4392.
12. Fromm, D. P.; Sundaramurthy, A.; Schuck, P. J.; Kino, G.; Moerner, W. E. Gap-Dependent Optical Coupling of Single Au-Bowtie Au Nanoantennas Resonant in the Visible. *Nano Lett.* **2004**, *4*, 957–961.
13. Lin, T.-R.; Chang, S.-W.; Chuang, S. L.; Zhang, Z.; Schuck, P. J. Coating Effect on Optical Resonance of Plasmonic Nanobowtie Antenna. *Appl. Phys. Lett.* **2010**, *97*, 063106.
14. Mastel, S.; Grefe, S. E.; Cross, G. B.; Taber, A.; Dhuey, S.; Cabrini, S.; Schuck, P. J.; Abate, Y. Real-Space Mapping of Nanoplasmonic Hotspots *via* Optical Antenna-Gap Loading. *Appl. Phys. Lett.* **2012**, *101*, 131102.
15. Hatab, N. A.; Hsueh, C.-H.; Gaddis, A. L.; Retterer, S. T.; Li, J.-H.; Eres, G.; Zhang, Z.; Gu, B. Free-Standing Optical Gold Bowtie Nanoantenna with Variable Gap Size for Enhanced Raman Spectroscopy. *Nano Lett.* **2010**, *10*, 4952–4955.
16. Nordlander, P. The Ring: A Leitmotif in Plasmonics. *ACS Nano* **2009**, *3*, 488–492.
17. Schelm, S.; Smith, G. B. Internal Electric Field Densities of Metal Nanoshells. *J. Phys. Chem. B* **2005**, *109*, 1689–1694.
18. Aizpurua, J.; Hanarp, P.; Sutherland, D. S.; Käll, M.; Bryant, G. W.; García de Abajo, F. J. Optical Properties of Gold Nanorings. *Phys. Rev. Lett.* **2003**, *90*, 057401.
19. Larsson, E. M.; Alegret, J.; Käll, M.; Sutherland, D. S. Sensing Characteristics of NIR Localized Surface Plasmon Resonances in Gold Nanorings for Application as Ultrasensitive Biosensors. *Nano Lett.* **2007**, *7*, 1256–1263.
20. Kim, S.; Jung, J.-M.; Choi, D.-G.; Jung, H.-T.; Yang, S.-M. Patterned Arrays of Au Rings for Localized Surface Plasmon Resonance. *Langmuir* **2006**, *22*, 7109–7112.
21. Huang, C.; Ye, J.; Wang, S.; Stakenborg, T.; Lagae, L. Gold Nanoring as a Sensitive Plasmonic Biosensor for on-Chip DNA Detection. *Appl. Phys. Lett.* **2012**, *100*, 173114.
22. Ahmed, A.; Gordon, R. Directivity Enhanced Raman Spectroscopy Using Nanoantennas. *Nano Lett.* **2011**, *11*, 1800–1803.
23. Wang, D.; Zhu, W.; Best, M. D.; Camden, J. P.; Crozier, K. B. Directional Raman Scattering from Single Molecules in the Feed Gaps of Optical Antennas. *Nano Lett.* **2013**, *13*, 2194–2198.
24. Auguié, B.; Barnes, W. L. Diffractive Coupling in Gold Nanoparticle Arrays and the Effect of Disorder. *Opt. Lett.* **2009**, *34*, 401–403.
25. Law, M.; Sirbuly, D. J.; Johnson, J. C.; Goldberger, J.; Saykally, R. J.; Yang, P. Nanoribbon Waveguides for Subwavelength Photonics Integration. *Science* **2004**, *305*, 1269–1273.
26. Maier, S. A.; Kik, P. G.; Atwater, H. A.; Meltzer, S.; Harel, E.; Koel, B. E.; Requicha, A. A. G. Local detection of electromagnetic energy transport below the diffraction limit in metal nanoparticle plasmon waveguides. *Nat. Mater.* **2003**, *2*, 229.
27. Huang, Y.; Duan, X.; Lieber, C. M. Directed Assembly of One-Dimensional Nanostructures into Functional Networks. *Science* **2001**, *291*, 630.
28. Katz, E.; Willner, I. *Angew. Chem.,* Integrated Nanoparticle-Biomolecule Hybrid Systems: Synthesis, Properties, and Applications. *Int. Ed.* **2004**, *43*, 6042.
29. Sepúlveda, B.; Angelomé, P. C.; Lechuga, L. M.; Liz-Marzán, L. M. LSPR-based nanobiosensors. *Nano Today* **2009**, *4*, 244.
30. D'Andrea, C.; Bochterle, J.; Toma, A.; Huck, C.; Neubrech, F.; Messina, E.; Fazio, B.; Marago, O. M.; Di Fabrizio, E.; Lamy De La Chapelle, M.; Gucciardi, P. G.; Pucci, A. Optical Nanoantennas for Multiband Surface-Enhanced Infrared and Raman Spectroscopy. *ACS Nano* **2013**, *7*, 3522–3531.

31. Kreibig, U.; Vollmer, M. *Optical Properties of Metal Clusters*; Springer: Berlin, 1995.
32. Johnson, P. B.; Christy, R. W. Optical Constants of the Noble Metals. *Phys. Rev. B* **1972**, *6*, 4370–4379.
33. Kahraman, M.; Aydn, Ö.; Çulha, M. Oligonucleotide-Mediated Au–Ag Core–Shell Nanoparticles. *Plasmonics* **2009**, *4*, 293–301.
34. Cao, Y.; Jin, R.; Mirkin, C. A. DNA-Modified Core–Shell Ag/Au Nanoparticles. *J. Am. Chem. Soc.* **2001**, *123*, 7961–7962.
35. Lim, D.-K.; Kim, I.-J.; Nam, J.-M. DNA-Embedded Au/Ag Core-Shell Nanoparticles. *Chem. Commun.* **2008**, 5312–5314.
36. Becker, J.; Zins, I.; Jakab, A.; Khalavka, Y.; Schubert, O.; Sönnichsen, C. Plasmonic Focusing Reduces Ensemble Linewidth of Silver-Coated Gold Nanorods. *Nano Lett.* **2008**, *8*, 1719–1723.
37. DeSantis, C. J.; Weiner, R. G.; Radmilovic, A.; Bower, M. M.; Skrabalak, S. E. Seeding Bimetallic Nanostructures as a New Class of Plasmonic Colloids. *J. Phys. Chem. Lett.* **2013**, *4*, 3072–3082.
38. Wang, L.; Kiya, A.; Okuno, Y.; Niidome, Y.; Tamai, N. Ultrafast Spectroscopy and Coherent Acoustic Phonons of Au–Ag Core–Shell Nanorods. *J. Chem. Phys.* **2011**, *134*, 054501–6.
39. Gómez-Graña, S.; Pérez-Juste, J.; Alvarez-Puebla, R. A.; Guerrero-Martínez, A.; Liz-Marzán, L. M. Self-Assembly of Au@Ag Nanorods Mediated by Gemini Surfactants for Highly Efficient SERS-Active Supercrystals. *Adv. Opt. Mater.* **2013**, *1*, 477–481.
40. Rivas, L.; Sanchez-Cortes, S.; García-Ramos, J. V.; Morcillo, G. Mixed Silver/Gold Colloids: A Study of Their Formation, Morphology, and Surface-Enhanced Raman Activity. *Langmuir* **2000**, *16*, 9722–9728.
41. Dengler, S.; Kübel, C.; Schwenke, A.; Ritt, G.; Eberle, B. Near- and Off-Resonant Optical Limiting Properties of Gold–Silver Alloy Nanoparticles for Intense Nanosecond Laser Pulses. *J. Opt.* **2012**, *14*, 075203.
42. Kho, K. W.; Dinish, U. S.; Kumar, A.; Olivo, M. Frequency Shifts in Sers for Biosensing. *ACS Nano* **2012**, *6*, 4892–4902.
43. Patra, P. P.; Kumar, G. V. P. Single-Molecule Surface-Enhanced Raman Scattering Sensitivity of Ag-Core Au-Shell Nanoparticles: Revealed by Bi-Analyte Method. *J. Phys. Chem. Lett.* **2013**, *4*, 1167–1171.
44. Siegfried, T.; Kind, M.; Terfort, A.; Martin, O. J. F.; Zharnikov, M.; Ballav, N.; Sigg, H. Reusable Plasmonic Substrates Fabricated by Interference Lithography: A Platform for Systematic Sensing Studies. *J. Raman Spectrosc.* **2013**, *44*, 170–175.
45. Sackmann, M.; Bom, S.; Balster, T.; Materny, A. Nanostructured Gold Surfaces as Reproducible Substrates for Surface-Enhanced Raman Spectroscopy. *J. Raman Spectrosc.* **2007**, *38*, 277–282.
46. Li, X.; Chen, G.; Yang, L.; Jin, Z.; Liu, J. Multifunctional Au-Coated TiO_2 Nanotube Arrays as Recyclable SERS Substrates for Multifold Organic Pollutants Detection. *Adv. Funct. Mater.* **2010**, *20*, 2815–2824.
47. Jih-Shang, H.; Kuan-Yu, C.; Shih-Jay, H.; Shih-Wei, C.; Wun-Shing, S.; Chi-Wen, K.; Wei-Yi, S.; Tai Yuan, L.; Hai-Pang, C.; Surojit, C.; Kuei-Hsien, C.; Li-Chyong, C. The Preparation of Silver Nanoparticle Decorated Silica Nanowires on Fused Quartz as Reusable Versatile Nanostructured Surface-Enhanced Raman Scattering Substrates. *Nanotechnology* **2010**, *21*, 025502.
48. Mahurin, S. M.; John, J.; Sepaniak, M. J.; Dai, S. A Reusable Surface-Enhanced Raman Scattering (SERS) Substrate Prepared by Atomic Layer Deposition of Alumina on a Multi-Layer Gold and Silver Film. *Appl. Spectrosc.* **2011**, *65*, 417–422.
49. Chirumamilla, M.; Toma, A.; Gopalakrishnan, A.; Das, G.; Zaccaria, R. P.; Krahne, R.; Rondanina, E.; Leoncini, M.; Liberale, C.; De Angelis, F.; Di Fabrizio, E. 3D Nanostar Dimers with a Sub-10-nm Gap for Single-/Few-Molecule Surface-Enhanced Raman Scattering. *Adv. Mater.* **2014**, *26*, 2353–2358.
50. Perassi, E. M.; Canali, L. R.; Coronado, E. A. Enhancement and Confinement Analysis of the Electromagnetic Fields inside Hot Spots. *J. Phys. Chem. C* **2009**, *113*, 6315–6319.
51. Perassi, E. M.; Coronado, E. A. The Structure, Energy, Confinement, and Enhancement of Hot Spots between Two Nanoparticles. *J. Phys. Chem. C* **2013**, *117*, 7744–7750.
52. Rakic, A. D.; Djurišic, A. B.; Elazar, J. M.; Majewski, M. L. Optical Properties of Metallic Films for Vertical-Cavity Optoelectronic Devices. *Appl. Opt.* **1998**, *37*, 5271–5283.
53. Alabastri, A.; Tuccio, S.; Giugni, A.; Toma, A.; Liberale, C.; Das, G.; Angelis, F. D.; Fabrizio, E. D.; Zaccaria, R. P. Molding of Plasmonic Resonances in Metallic Nanostructures: Dependence of the Non-Linear Electric Permittivity on System Size and Temperature. *Materials* **2013**, *6*, 4879–4910.
54. Kneipp, K. M. M.; Kneipp, H. *Surface-Enhanced Raman Scattering. Physics and Applications*; Springer: New York, 2007.
55. Jackson, J. B.; Halas, N. J. Surface-Enhanced Raman Scattering on Tunable Plasmonic Nanoparticle Substrates. *Proc. Natl. Acad. Sci. U.S.A.* **2004**, *101*, 17930–17935.
56. Osawa, M.; Matsuda, N.; Yoshii, K.; Uchida, I. Charge Transfer Resonance Raman Process in Surface-Enhanced Raman Scattering from p-Aminothiophenol Adsorbed on Silver: Herzberg-Teller Contribution. *J. Phys. Chem.* **1994**, *98*, 12702–12707.
57. Shegai, T.; Miljković, V. D.; Bao, K.; Xu, H.; Nordlander, P.; Johansson, P.; Käll, M. Unidirectional Broadband Light Emission from Supported Plasmonic Nanowires. *Nano Lett.* **2011**, *11*, 706–711.
58. Fraire, J. C.; Perez, L. A.; Coronado, E. A. Rational Design of Plasmonic Nanostructures for Biomolecular Detection: Interplay between Theory and Experiments. *ACS Nano* **2012**, *6*, 3441–3452.
59. Han, S.-Y.; Guo, Q.-H.; Xu, M.-M.; Yuan, Y.-X.; Shen, L.-M.; Yao, J.-L.; Liu, W.; Gu, R.-A. Tunable Fabrication on Iron Oxide/Au/Ag Nanostructures for Surface Enhanced Raman Spectroscopy and Magnetic Enrichment. *J. Colloid Interface Sci.* **2012**, *378*, 51–57.
60. Hu, X.; Wang, T.; Wang, L.; Dong, S. Surface-Enhanced Raman Scattering of 4-Aminothiophenol Self-Assembled Monolayers in Sandwich Structure with Nanoparticle Shape Dependence: Off-Surface Plasmon Resonance Condition. *J. Phys. Chem. C* **2007**, *111*, 6962–6969.
61. Liu, G.-K.; Hu, J.; Zheng, P.-C.; Shen, G.-L.; Jiang, J.-H.; Yu, R.-Q.; Cui, Y.; Ren, B. Laser-Induced Formation of Metal–Molecule–Metal Junctions between Au Nanoparticles as Probed by Surface-Enhanced Raman Spectroscopy. *J. Phys. Chem. C* **2008**, *112*, 6499–6508.
62. Zhou, Q.; Li, X.; Fan, Q.; Zhang, X.; Zheng, J. Charge Transfer between Metal Nanoparticles Interconnected with a Functionalized Molecule Probed by Surface-Enhanced Raman Spectroscopy. *Angew. Chem., Int. Ed.* **2006**, *45*, 3970–3973.
63. Uetsuki, K.; Verma, P.; Yano, T.-a.; Saito, Y.; Ichimura, T.; Kawata, S. Experimental Identification of Chemical Effects in Surface Enhanced Raman Scattering of 4-Aminothiophenol. *J. Phys. Chem. C* **2010**, *114*, 7515–7520.
64. Zuloaga, J.; Nordlander, P. On the Energy Shift between Near-Field and Far-Field Peak Intensities in Localized Plasmon Systems. *Nano Lett.* **2011**, *11*, 1280–1283.
65. Biagioni, P.; Huang, J. S.; Hecht, B. Nanoantennas for Visible and Infrared Radiation. *Rep. Prog. Phys.* **2012**, *75*, 024402.
66. Oh, Y.-J.; Jeong, K.-H. Glass Nanopillar Arrays with Nanogap-Rich Silver Nanoislands for Highly Intense Surface Enhanced Raman Scattering. *Adv. Mater.* **2012**, *24*, 2234–2237.
67. Im, H.; Bantz, K. C.; Lee, S. H.; Johnson, T. W.; Haynes, C. L.; Oh, S.-H. Self-Assembled Plasmonic Nanoring Cavity Arrays for SERS and LSPR Biosensing. *Adv. Mater.* **2013**, *25*, 2678–2685.
68. Hennemann, L. E.; Kolloch, A.; Kern, A.; Mihaljevic, J.; Boneberg, J.; Leiderer, P.; Meixner, A. J.; Zhang, D. Assessing the Plasmonics of Gold Nano-Triangles with Higher Order Laser Modes. *Beilstein J. Nanotechnol.* **2012**, *3*, 674–683.
69. Liu, H.; Zhang, L.; Lang, X.; Yamaguchi, Y.; Iwasaki, H.; Inouye, Y.; Xue, Q.; Chen, M., Single Molecule Detection from a Large-Scale SERS-Active Au79Ag21 Substrate. *Sci. Rep.* **2011**, *1*.
70. Aroca, R. F. Plasmon Enhanced Spectroscopy. *Phys. Chem. Chem. Phys.* **2013**, *15*, 5355–5363.